Efficient Perovskite Hybrid Solar Cells via Ionomer Interfacial Engineering

Kai Wang, Chang Liu, Chao Yi, Long Chen, Jiahua Zhu, R. A. Weiss, and Xiong Gong**

The surface of the solution-processed methylammonium lead tri-iodide ($CH_3NH_3PbI_3$) perovskite layer in perovskite hybrid solar cells (pero-HSCs) tends to become rough during operation, which inevitably leads to deterioration of the contact between the perovskite layer and the charge-extraction layers. Moreover, the low electrical conductivity of the electron extraction layer (EEL) gives rises to low electron collection efficiency and severe charge carrier recombination, resulting in energy loss during the charge-extraction and -transport processes, lowering the efficiency of pero-HSCs. To circumvent these problems, we utilize a solution-processed ultrathin layer of a ionomer, 4-lithium styrenesulfonic acid/styrene copolymer (LiSPS), to re-engineer the interface of $CH_3NH_3PbI_3$ in planar heterojunction (PHJ) pero-HSCs. As a result, PHJ pero-HSCs are achieved with an increased photocurrent density of 20.90 mA cm^{-2}, an enlarged fill factor of 77.80%, a corresponding enhanced power conversion efficiency of 13.83%, high reproducibility, and low photocurrent hysteresis. Further investigation into the optical and electrical properties and the thin-film morphologies of $CH_3NH_3PbI_3$ with and without LiSPS, and the photophysics of the pero-HSCs with and without LiSPS are shown. These demonstrate that the high performance of the pero-HSCs incorporated with LiSPS can be attributed to the reduction in both the charge carrier recombination and leakage current, as well as more efficient charge carrier collection, filling of the perforations in $CH_3NH_3PbI_3$, and a higher electrical conductivity of the LiSPS thin layer. These results demonstrate that our method provides a simple way to boost the efficiency of pero-HSCs.

1. Introduction

Economically and efficiently harnessing solar energy via photovoltaic devices has been presented as one of the most promising solutions to the global energy crisis.[1–3] Recently, new light has been shed on the burgeoning methylammonium lead tri-iodide ($CH_3NH_3PbI_3$) perovskite hybrid solar cells (pero-HSCs) because of the superior optical and electrical properties of the perovskite materials[4,5] and the low-cost fabrication process and high power conversion efficiencies (PCEs) of pero-HSCs.[6,7] Mesoporous structured (MS),[8] planar heterojunction (PHJ),[9] and bulk heterojunction (BHJ)[10,11] pero-HSCs have been invented to address one of the more fundamental issues, namely, the fact that the electron diffusion length is shorter than that of the holes ($L_{\text{eff, e–}}/L_{\text{eff, h+}} < 1$) in $CH_3NH_3PbI_3$ perovskite,[12] for further boosting the PCEs of pero-HSCs. However, so far no solution has been found for the whole problem due to the poor electron-extraction efficiency from the electron-extraction layer (EEL) to the electrode.[13,14] In fact, the electrical conductivities of a TiO_x EEL in MS pero-HSCs and phenyl-C_{61}-butyric acid methyl ester ($PC_{61}BM$) EEL in PHJ pero-HSCs are several orders of magnitude lower than those of the hole-extraction layer (HEL) counterparts,[15–20] resulting in an inferior electron-collection efficiency, lower short-circuit current density (J_{SC}), and lower fill factor (FF).[11,21] On the other hand, it has been reported that the contact between the perovskite layer and the EEL was poor due to the rough surface of the solution-processed perovskite layer,[22,23] which inevitably deteriorates the electron-extraction efficiency, creates charge-carrier recombination, and simultaneously introduces large leakage currents.[24–26] In order to circumvent these problems, studies have been focused on the interfacial modification of the contact between the EEL and the cathode. Improved electron transport towards the cathode has been observed from pero-HSCs incorporated with a thin layer of thermal-evaporated LiF, bathocuproin (BCP), and fullerene (C_{60}), which was inserted between the $PC_{61}BM$ EEL and the electrodes.[27] Surprisingly, however, the manipulation of the interface between the solution-processed $CH_3NH_3PbI_3$ perovskite layer and the $PC_{61}BM$ EEL has rarely been addressed. In this scenario, we employ a solution-processed ionomer, 4-lithium styrenesulfonic acid/styrene copolymer (LiSPS), to re-engineer the interface between the solution-processed $CH_3NH_3PbI_3$ perovskite layer and the $PC_{61}BM$ EEL. The introduction of such highly ionic, electrically conductive LiSPS to optimize the carrier-transport pathway results in enhanced electron-collection efficiency. Moreover, the LiSPS possesses a good wettability

K. Wang, C. Liu, C. Yi, Prof. R. A. Weiss, Prof. X. Gong
Department of Polymer Engineering
College of Polymer Science and Polymer Engineering
The University of Akron
Akron, OH 44325, USA
E-mail: rweiss@uakron.edu; xgong@uakron.edu
L. Chen, Dr. J. Zhu
Department of Chemical & Biomolecular Engineering
The University of Akron
Akron, OH 44325, USA

DOI: 10.1002/adfm.201503160

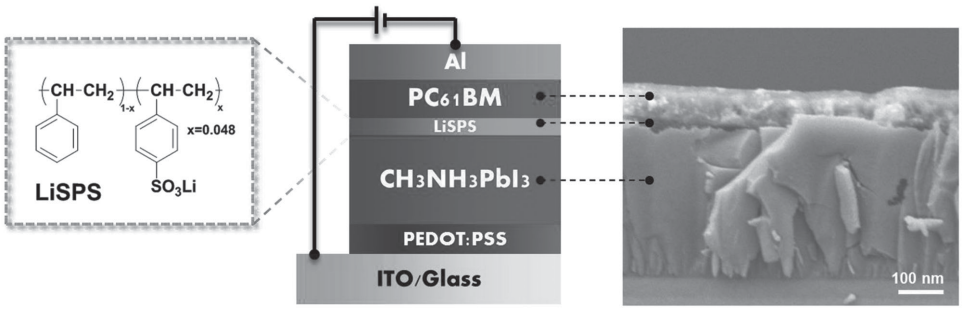

Figure 1. Molecular structure of LiSPS (left), device structure of PHJ pero-HSCs incorporated with a LiSPS layer (middle) and cross-sectional SEM images of glass substrate/$CH_3NH_3PbI_3$/LiSPS/$PC_{61}BM$ (right).

on the surface of organic–inorganic composites, which would facilitate the LiSPS ionomers to fill in the pin-holes of the solution-processed $CH_3NH_3PbI_3$, resulting in a smoothened surface of the $CH_3NH_3PbI_3$ perovskite. As a result, an enhanced J_{SC} of 20.90 mA cm^{-2}, an open-circuit voltage (V_{OC}) of 0.85 V, an enlarged FF of 77.80% and a correspondingly enhanced PCE of 13.83%, with a high device reproducibility and low photocurrent hysteresis were observed from these pero-HSCs.

2. Results and Discussions

Figure 1 presents the PHJ pero-HSCs device configuration of ITO/PEDOT:PSS/$CH_3NH_3PbI_3$/LiSPS/$PC_{61}BM$/Al, where the indium tin oxide (ITO) acts as the anode, the $CH_3NH_3PbI_3$ film acts as the light absorber, the (poly(3,4-ethylenedioxythiophene):polystyrene sulfonate) (PEDOT:PSS) acts as the hole-transport layer (HTL), $PC_{61}BM$ acts as the EEL, and Al acts as the cathode. The cross-sectional scanning electron microscopy (SEM) images of $CH_3NH_3PbI_3$/LiSPS/$PC_{61}BM$ and the chemical structure of LiSPS are also shown in Figure 1. Each layer can clearly be seen in the cross-sectional SEM image of $CH_3NH_3PbI_3$/LiSPS/$PC_{61}BM$. Pero-HSCs with a device structure of ITO/PEDOT:PSS/$CH_3NH_3PbI_3$/$PC_{61}BM$/Al were also fabricated as the control and characterized for comparison studies.

The LiSPS ionomer[28–31] was selected to re-engineer the surface of solution-processed $CH_3NH_3PbI_3$ because of its high ionic (Li^+) electrical conductivity[32–34] and the fact that the ionic nanodomains can act as physical crosslinkers in the ionomer, forming robust thin films after solvent drying.[35] The high ionic electrical conductivity of the ionomer could facilitate charge carriers to be transported from the $CH_3NH_3PbI_3$ layer to the $PC_{61}BM$ EEL[36] and the robust thin films would allow the upper $PC_{61}BM$ EEL to be solution-processed without destroying the ionomer layer. Moreover, the LiSPS ionomer was selected because of its good wettability on the surface of organic–inorganic composites,[35] which would facilitate the ionomer to fill in the pin-holes of the solution-processed $CH_3NH_3PbI_3$ layer, resulting in a good contact between the $CH_3NH_3PbI_3$ layer and the $PC_{61}BM$ EEL. On the other hand, using a lightly sulfonated polystyrene (SPS) as the anion in the LiSPS ionomer, which possesses the relatively low pK_a of sulfonic acid (ca. 1.0),[37] will allow it to achieve a more complete neutralization by the Li^+ cations. The effect of ionic associations is much greater for sulfonate ionomers compared to other ionomers, such as organic carboxylic acids (pK_a around 4–5).[38] As a consequence, a more robust ionomer thin film can be realized by using SPS as the anionic polymer.

Figure 2a presents the current density versus voltage (J–V) characteristics of pero-HSCs with and without an incorporated LiSPS layer (represented as pero-HSCs W/ LiSPS and pero-HSCs W/O LiSPS, respectively). Under AM 1.5-simulated white illumination with a light intensity of 100 mW cm^{-2}, the pero-HSCs W/O LiSPS exhibited a V_{OC} of 0.85 ± 0.03 V, a J_{SC} of 15.33 ± 1.54 mA cm^{-2}, a FF of 72.40 ± 1.41%, and a corresponding PCE of 9.43 ± 1.21%. These device performance parameters are comparable to previously reported values for pero-HSCs with a similar device structure.[39,40] The pero-HSCs W/ LiSPS exhibited a V_{OC} of 0.85 ± 0.02 V, a J_{SC} of 20.90 ± 0.91 mA cm^{-2}, a FF of 77.80 ± 0.80%, and a corresponding PCE of 13.83 ± 0.35%. The fact that the V_{OC} values of the pero-HSCs W/ LiSPS and the pero-HSCs W/O LiSPS are almost identical indicates that the introduction of LiSPS on the surface of $CH_3NH_3PbI_3$ layer does not induce a dipole.[41] However, the dramatically enhanced J_{SC} and FF with incorporated LiSPS resulted in a more than 45% augmentation of the PCE. The enhanced J_{SC} indicates that less of the separated electrons

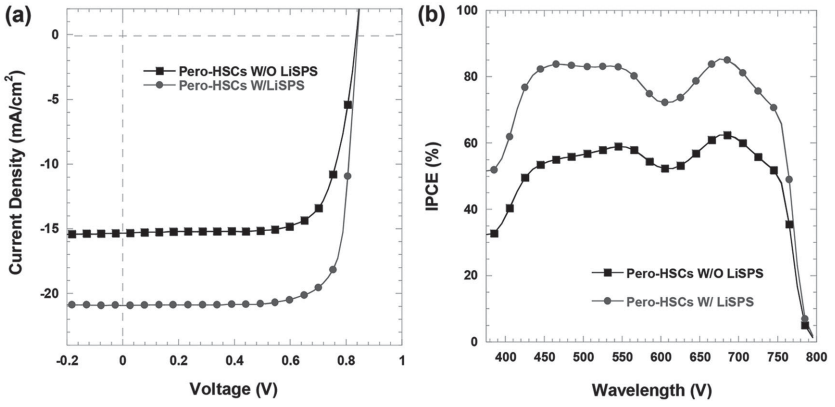

Figure 2. a) The J–V characteristics of pero-HSCs under AM1.5 simulated illumination, b) the incident photon to current efficiency (IPCE) spectra of pero-HSCs.

are lost during the electron-extraction and -transport processes from the $CH_3NH_3PbI_3$ layer though the LiSPS/$PC_{61}BM$ layer to the corresponding Al electrode.[20] The enhanced FF indicates that more balanced charge carriers are collected at the electrodes and less charge-carrier recombination takes place after the introduction of the LiSPS interfacial layer.[11,24,26]

In order to understand the underlying physics of the high J_{SC} and large FF from the pero-HSCs W/ LiSPS, the series resistance (R_S) and shunt resistance (R_{SH}) were estimated from the slope of the *J–V* curves under one sun illumination at open-circuit and short-circuit conditions, respectively. For solar cells, keeping the R_S as low as possible is of paramount importance because a larger R_S will decrease the J_{SC}, V_{OC}, FF, and consequently the PCE.[42,43] Contrarily to the R_S, the R_{SH} must be as high as possible to avoid current loss at the junction and to maintain a high photocurrent as well as good solar cell performance.[44] The R_S from the pero-HSCs W/ LiSPS was 0.32 kΩ cm^2, which is smaller than the 1.01 kΩ cm^2 that was obtained for the pero-HSCs W/O LiSPS. The lower R_S for the pero-HSCs W/ LiSPS probably originated from a smaller contact resistance and a lower bulk resistance after introduction of the LiSPS interfacial layer. The lower R_S also indicates that high currents can flow through the cells at low applied voltages.[45] On the other hand, the R_{SH} from the pero-HSCs W/ LiSPS was 311.08 kΩ cm^2, which is much larger than the 199.71 kΩ cm^2 obtained for the pero-HSCs W/O LiSPS. The larger R_{SH} indicates that the leakage currents are minimized, resulting in a high J_{SC} for the pero-HSCs W/ LiSPS. Moreover, such large R_{SH} and small R_S values, in particular, the reduced parasitic resistance at the $CH_3NH_3PbI_3$/LiSPS/$PC_{61}BM$ interface,[46] resulted in a large FF for the pero-HSCs W/ LiSPS.

Figure 2b presents the incident photon-to-electron conversion efficiency (IPCE) spectra of the pero-HSCs. The IPCE specifies the ratio of extracted electrons to incident photons at a given wavelength. Both pero-HSCs W/O LiSPS and pero-HSCs W/ LiSPS shared a typical IPCE pattern of PHJ pero-HSCs, where the generation of the photocurrent started at 1.56 eV, which is in good agreement with the bandgap of $CH_3NH_3PbI_3$.[5,6] The steep onset at 790 nm is probably related to the specific interaction of the perovskite with the fullerene molecules and the dip at 630 nm probably results from the reduced absorption of the perovskite layer due to the reflection effect.[47,48] Moreover, it was found that the pero-HSCs W/ LiSPS possessed an enhanced photoresponse in comparison with the pero-HSCs W/O LiSPS. The pero-HSCs W/ LiSPS showed a wide photoresponse from the visible to the near-infrared range, with an IPCE of over 80% for wavelengths ranging from 430 to 560 nm and from 650 to 710 nm, whereas the pero-HSCs W/O LiSPS had an IPCE value below 60% over the whole spectral region. Integrating the overlap of the IPCE spectrum with the AM1.5G solar photon flux yielded photocurrent densities of 19.08 mA cm^{-2} and 13.51 mA cm^{-2} for the pero-HSCs W/ LiSPS and the pero-HSCs W/O LiSPS, respectively. These values are in good agreement with those obtained from the *J–V* characteristics (Figure 2a).

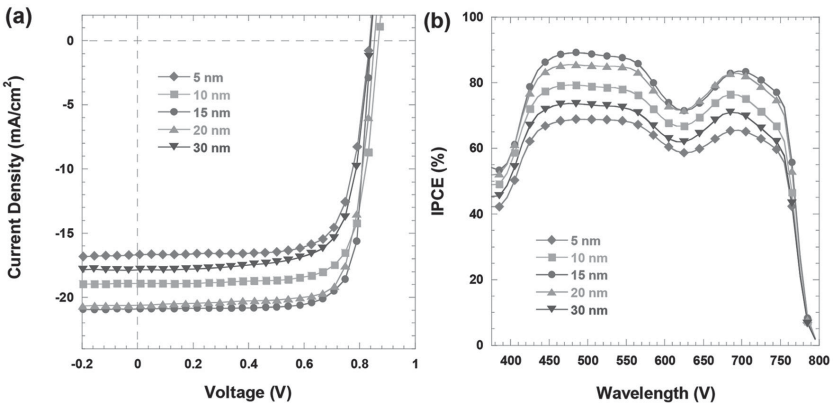

Figure 3. a) *J–V* characteristics and b) IPCE spectra of pero-HSCs with LiSPS layers of different thicknesses.

To further optimize the device performance of pero-HSCs, pero-HSCs with an LiSPS layer of different thicknesses were studied. **Figure 3**a,b presents the *J–V* characteristics and IPCE spectra of pero-HSCs with different LiSPS layer thicknesses. A V_{OC} of 0.85 V was observed for pero-HSCs incorporating a LiSPS layer with a thickness smaller than 30 nm. However, a dramatically decreased V_{OC} of 0.77 V was observed for pero-HSCs incorporating a LiSPS layer that was larger than 30 nm. The decreased V_{OC} probably originated from the reduced carrier concentration due to the decreased electrical conductivity in thicker LiSPS layers.[34,49] The FF initially increased from 74.80% to 78.30% (which was the highest achieved) as the thickness of the LiSPS layer increased from 5 nm to 20, and then decreased to 71.60% nm as the thickness of the LiSPS layer was further increased to 30 nm. A similar trend was also found for the J_{SC}. The J_{SC} values initially increased from 16.63 mA cm^{-2} to 20.90 mA cm^{-2} as the thickness of the LiSPS layer increased from 5 nm to 15 nm, and then decreased to 15.22 mA cm^{-2} as the thickness of the LiSPS layer was further increased to 30 nm, as shown in **Table 1**. The IPCE of the pero-HSCs was further investigated to verify the differences in J_{SC}. All pero-HSCs possessed a similar IPCE pattern from 375 nm to 800 nm. Integrating the overlap of the IPCE spectrum with the AM1.5G solar photon flux yielded the J_{SC} for each device. Table 1 summarizes the integrated J_{SC} values. These integrated J_{SC} values

Table 1. Effect of LiSPS thickness on the device performance.

Thickness of LiSPS [nm]	V_{OC} [V]	J_{SC}* [a)] [mA cm^{-2}]	J_{SC}# [a)] [mA cm^{-2}]	FF [%]	PCE [%]
0	0.85	15.33	13.51	72.40	9.43
5	0.84	16.63	15.47	74.80	10.49
10	0.85	18.98	17.73	77.70	12.54
15	0.85	20.90	19.67	77.80	13.83
20	0.84	20.61	19.25	78.30	13.60
30	0.77	15.22	13.51	71.60	8.36

[a)] J_{SC}* from *J–V* characteristics; J_{SC}# from IPCE spectra.

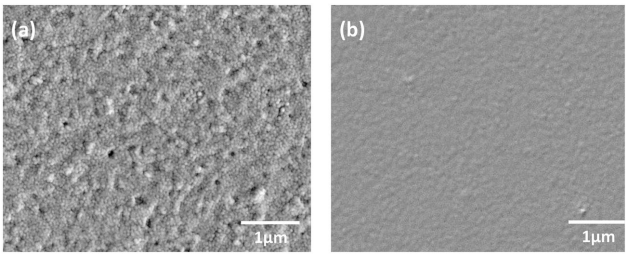

Figure 4. Top view SEM images of a) a pristine $CH_3NH_3PbI_3$ thin film and b) a $CH_3NH_3PbI_3$/LiSPS thin film.

were consistent with those observed from the *J–V* characteristics (Figure 3a). The dramatic differences found for the J_{SC} of pero-HSCs with different thicknesses of the LiSPS layer are then probably related to the coverage of LiSPS on the surface of the $CH_3NH_3PbI_3$ layer and the variance in the electrical conductivities of the LiSPS layer. If the thickness of the LiSPS layer is smaller than 10 nm, the $CH_3NH_3PbI_3$ layer is not completely covered by the LiSPS layer. As the thickness of the LiSPS layer is increased to more than 10 nm, the $CH_3NH_3PbI_3$ layer starts to become completely covered by the LiSPS layer. Such interfacial modification lead to a higher performance of the pero-HSCs. However, as the thickness is further increased, the electrical conductivity of the LiSPS layer dramatically decreases, resulting in a deteriorated performance of pero-HSCs with a LiSPS layer of 30 nm or higher.

Figure 4 compares top-view SEM images of a pristine $CH_3NH_3PbI_3$ thin film and a $CH_3NH_3PbI_3$ thin film covered with a 15-nm LiSPS layer. As shown in Figure 4a, pin-holes can be found on the surface of the $CH_3NH_3PbI_3$ thin film. It should be noted that pinholes formed in the perovskite layer can compromise the efficiency by introducing shunt paths in the device.[50] In contrast, no obvious pinholes were observed in the $CH_3NH_3PbI_3$/LiSPS thin film (Figure 4b), which indicates that the LiSPS layer has filled the pinholes in the $CH_3NH_3PbI_3$ layer. Thus, the interface between the $CH_3NH_3PbI_3$ layer and the $PC_{61}BM$ EEL was thoroughly modified by the LiSPS layer. Therefore, the trap-induced charge carrier recombination was decreased and the filled-in perforations by LiSPS resulted in a reduced leakage current, consequently, enhancing the photocurrent of the pero-HSCs W/ LiSPS.[51]

Figure 5 shows the atomic force microscopy (AFM) topographical images of a pristine $CH_3NH_3PbI_3$ thin film, a $CH_3NH_3PbI_3$ thin film partially covered by a LiSPS ultrathin layer, and a $CH_3NH_3PbI_3$ thin film completely covered by a LiSPS ultrathin layer. The pristine $CH_3NH_3PbI_3$ thin film shows a relatively large root-mean-square (RMS) roughness (*R*q) of 10.5 nm; the partially covered $CH_3NH_3PbI_3$ thin film shows a smaller *R*q of 3.2 nm; the completely covered $CH_3NH_3PbI_3$ thin film shows the smallest *R*q of 1.0 nm. These results indicate that the LiSPS ultrathin layer can significantly smoothen the rough surface of the $CH_3NH_3PbI_3$ thin film. In addition, from the phase images it can be seen that both the pristine $CH_3NH_3PbI_3$ thin film and the completely covered $CH_3NH_3PbI_3$ thin film show a one-phase pattern, whereas the partially covered $CH_3NH_3PbI_3$ thin film shows a two-phase pattern. These results indicate that the pin-holes of the $CH_3NH_3PbI_3$ thin film can be fully filled by the LiSPS ionomers. In consequence, by using a LiSPS ultrathin layer, the contact between the $CH_3NH_3PbI_3$ layer and the $PC_{61}BM$ EEL is optimized due to the reduced amount of pinholes.

Impedance spectroscopy (IS) was further used to estimate the electrical conductive properties of the LiSPS layer. **Figure 6**a presents the Nyquist plots of Al/$PC_{61}BM$/ITO and Al/LiSPS/ITO diodes, where the thickness of $PC_{61}BM$ was 100 nm in accordance with that in the pero-HSCs, and the thicknesses of the LiSPS layer were 5 nm, 10 nm, 15 nm, 20 nm, and 30 nm. In the above diodes, the ITO and high-work function Al were used to form the ohmic contact for minimization of the sheet resistance.

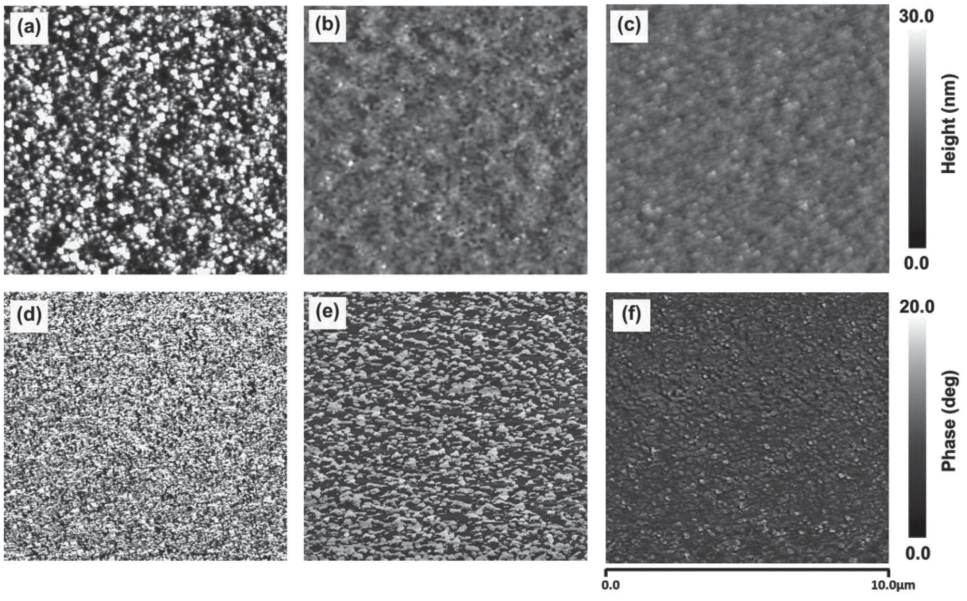

Figure 5. a–c) Tapping-mode AFM height images and d–f) corresponding AFM phase images of a pristine $CH_3NH_3PbI_3$ layer (a,d), a $CH_3NH_3PbI_3$ layer partially covered by LiSPS (b,e), and a $CH_3NH_3PbI_3$ layer completely covered by LiSPS (c,f).

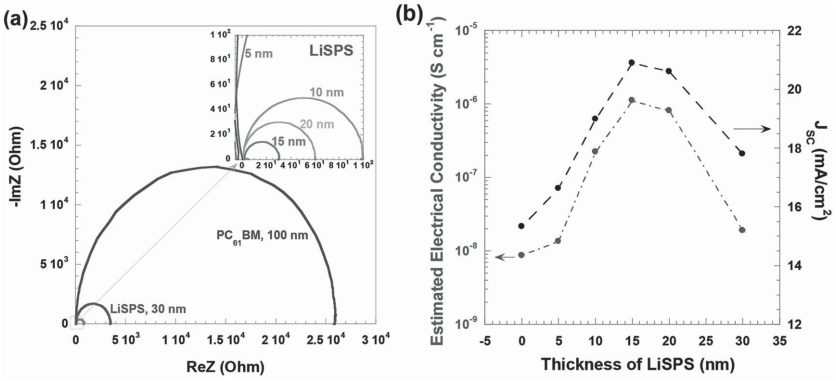

Figure 6. a) Nyquist plots of Al/$PC_{61}BM$/ITO and Al/LiSPS/ITO diodes, b) estimated electrical conductivity of the LiSPS layer, and J_{SC} of pero-HSCs W/ LiSPS versus the LiSPS layer with different thicknesses.

The $PC_{61}BM$ showed a large charge-transfer resistance (R_{CT}) of 2.6×10^4 Ω, whereas the R_{CT} of the 30-nm LiSPS layer was much lower (3.4×10^3 Ω). The inset in Figure 6a shows an enlarged Nyquist plot for the LiSPS layer with a thickness from 5 nm to 20 nm. Interestingly, as the thickness increases from 5 nm to 15 nm, the R_{CT} decreased eccentrically, which is probably due to unique polymer chain movements in the ultrathin layer or the complicated interaction between the polymer chain segment and the counter ions.[52,53] The electrical conductivities of $PC_{61}BM$ with a thickness of 100 nm and LiSPS with different thicknesses were further estimated. The correlation between the estimated electrical conductivities of the LiSPS layer and the J_{SC} values of pero-HSCs W/ LiSPS are shown in Figure 6b. The strikingly similar trends indicates that the electrical conductivity of the LiSPS interfacial modification layer plays an important role in the electron extraction and transport processes and therefore in the J_{SC} and PCE of pero-HSCs W/LiSPS. By inserting such a highly electrically conductive LiSPS interfacial layer, optimized contact between the $CH_3NH_3PbI_3$ layer and the $PC_{61}BM$ EEL is realized, which is more favorable for electrons being directly transported form the $CH_3NH_3PbI_3$ layer to the $PC_{61}BM$ EEL through the highly electrical conductive LiSPS layer rather than through the tunneling effect.[54]

To further investigate the role of the LiSPS interfacial modification layer in enhancing the PCE, the light-intensity dependence of J_{SC} and V_{OC} were further investigated. In solar cells, if the mean drift length of the electron or the hole (or both) is smaller than the thickness of the photoactive layer, geminate recombination needs to be considered.[55] Typically, the charge drift length in the $CH_3NH_3PbI_3$ layer is around 100 nm,[11] which is smaller than the thickness (300 nm) of the $CH_3NH_3PbI_3$ layer. The recombination kinetics can be illustrated by investigating the variations in the J_{SC} and V_{OC} values as a function of the light intensity. **Figure 7**a represents the steady-state light intensity dependence of J_{SC} for pero-HSCs with and without LiSPS. Both pero-HSCs show a power-law dependence of J_{SC} on the incident light intensity, indicating no significant energy barrier in the pero-HSCs.[56] However, the pero-HSCs W/O LiSPS exhibited a slightly non-linear dependence of J_{SC} on the light intensity with a coefficient $\alpha = 0.93$. The pero-HSCs W/ LiSPS, however, exhibited a near-linear dependence of J_{SC} on the light intensity with a coefficient $\alpha = 0.97$ according to the power-law fit:[57] $J_{SC} \propto I^{\alpha}$, where I is the light intensity. The approximately linear dependence of J_{SC} on the light intensity for pero-HSCs indicates that the nongeminate recombination in pero-HSCs is weak. This observation is consistent with previous reports.[58,59] The smaller deviation from $\alpha = 1$ in the pero-HSCs W/ LiSPS as opposed to that for the pero-HSCs W/O LiSPS indicates that almost all the charge carriers have been removed prior to charge recombination, which might be due to the high electrical conductivity of the LiSPS layer. Figure 7b represents the steady-state light-intensity

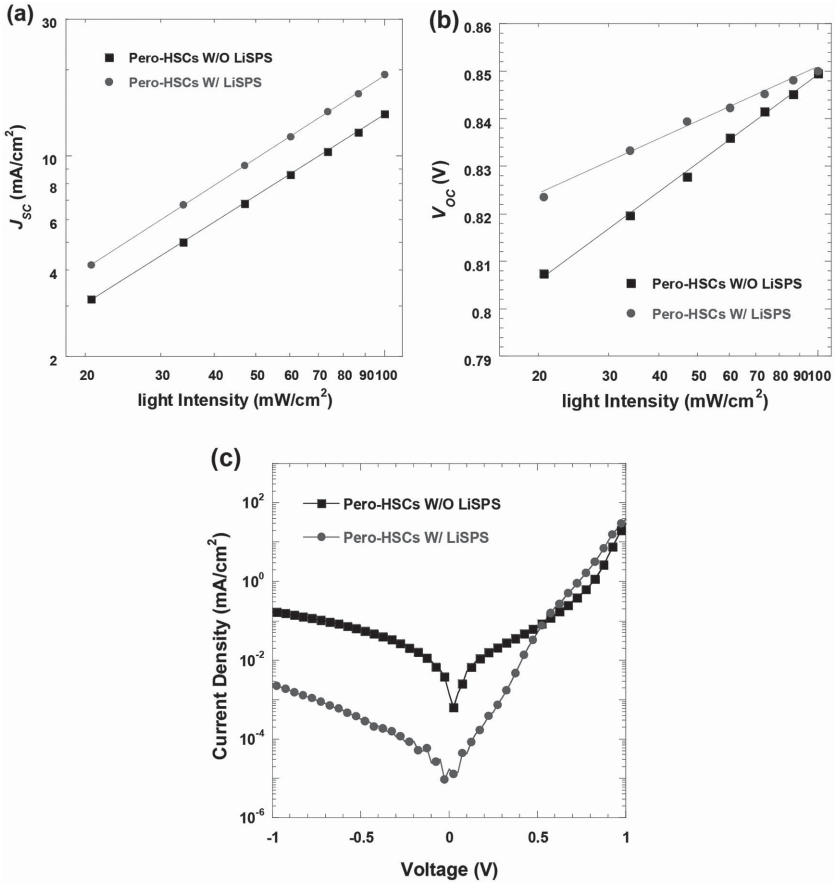

Figure 7. Light intensity dependence of a) J_{SC} and b) V_{OC}. c) *J–V* characteristics of pero-HSCs measured in the dark.

dependence of V_{OC} for the pero-HSCs with and without LiSPS. The relation between V_{OC} and the light intensity can be described as $V_{OC} \propto S \ln(I)$,[57] where S is the slope. Both pero-HSCs exhibited a semi-logarithmic plot of V_{OC} as a function of the light intensity. The V_{OC} of pero-HSCs W/O LiSPS was strongly dependent on the light intensity, with a slope, S of 2.48 k_BT/q (ca. 0.062), where k_B is the Boltzmann constant, q is the elementary charge, and T is the temperature in Kelvin. The pero-HSCs W/ LiSPS possessed a slope of 1.52 k_BT/q, which is smaller than that of the pero-HSCs W/O LiSPS. A smaller slope implies a reduced trap-assisted charge carrier recombination in the pero-HSCs W/ LiSPS.[60,61] The decreased charge carrier recombination in the pero-HSCs W/ LiSPS probably originated from the enlarged shunt resistance due to the passivated trap states by the LiSPS ionomer.

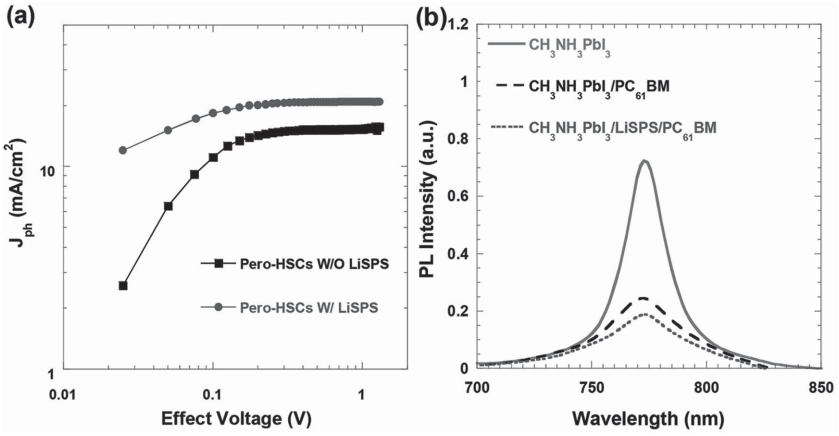

Figure 8. a) Photocurrent density–effective voltage (J_{ph}–V_{eff}) characteristics of pero-HSCs. b) Photoluminescence spectra of pristine $CH_3NH_3PbI_3$, $CH_3NH_3PbI_3/PC_{61}BM$, and $CH_3NH_3PbI_3$/LiSPS/$PC_{61}BM$.

Figure 7c exhibits the J–V characteristics of pero-HSCs in the dark. Under a reverse bias of −1 V, the pero-HSCs W/O LiSPS showed a large dark current density of 0.17 mA cm^{-2}, which was about 100 times larger than that of the pero-HSCs W/ LiSPS (2.3×10^{-3} mA cm^{-2}). Such huge difference in dark current indicates that the LiSPS interfacial layer plays a crucial role in perforating and passivating the trap states within the perovskite layer.[62] As a result, a high J_{SC} is observed for the pero-HSCs W/ LiSPS.

Figure 8a shows the net photocurrent–effective applied voltage (J_{ph}–V_{eff}) characteristics of pero-HSCs, with $J_{ph} = J_L - J_D$, where J_L and J_D are the current density under illumination and in the dark, respectively. The $V_{eff} = V_0 - V$, where V_0 is the voltage at which $J_{ph} = 0$ and V is the applied voltage. At a large reverse voltage ($V_{eff} \geq 1.2$ V), J_{ph} was saturated for pero-HSCs with and without LiSPS, suggesting that all of the photogenerated excitons were dissociated into free charge carriers and being collected by the electrodes.[63,64] In this case, the saturation current density, J_{sat}, was limited by the absorbed incident photo flux and charge transport within the pero-HSCs. It was found that the $CH_3NH_3PbI_3$ layer with and without added LiSPS layer possessed identical absorption properties. However, the pero-HSCs W/O LiSPS and the pero-HSCs W/ LiSPS showed a J_{sat} of 15.38 mA cm^{-2} and 20.85 mA cm^{-2}, respectively. Thus, the increased J_{sat} can be attributed to the effective charge-carrier transport and collection for the pero-HSCs W/ LiSPS.[65] In the low effective voltage range, namely $V_{eff} < 0.1$ V, the J_{ph}–V_{eff} characteristics of the two pero-HSCs showed distinct differences. The pero-HSCs W/O LiSPS showed a smaller value of J_{ph}/J_{sat} than that of the pero-HSCs W/ LiSPS. For example, at the maximum power output condition of $V_{eff} = 0.08$ V, the J_{ph}/J_{sat} values were 62.3% and 83.4% for the pero-HSCs W/O LiSPS and the pero-HSCs W/ LiSPS, respectively. As the ratio of J_{ph}/J_{sat} is essential for the exciton-dissociation efficiency and charge-carrier collection efficiency, a decreased J_{ph}/J_{sat} indicates either that the charge-carrier collection efficiency is reduced or that the exciton-dissociation efficiency is reduced.[63] If the charge-carrier collection efficiency is reduced, non-geminate recombination rather than exciton-dissociation will be dominant in the photocurrent generation process, which results in a low FF. The superior J_{ph}–V_{eff} characteristics of the pero-HSCs W/ LiSPS clearly demonstrate that the LiSPS layer can suppress the geminate recombination even at low effective voltage, where the maximum power output condition of solar cells generally takes place.[66]

In order to further understand the underlying device performance of the pero-HSCs W/O LiSPS and the pero-HSCs W/ LiSPS, photoluminescence (PL) studies of pristine $CH_3NH_3PbI_3$, $CH_3NH_3PbI_3/PC_{61}BM$, and $CH_3NH_3PbI_3$/LiSPS/$PC_{61}BM$ thin films were conducted. Figure 8b displays the PL spectra of different thin films. A typical PL peak at around 775 nm was observed in the pristine $CH_3NH_3PbI_3$ thin film. However, a more striking PL-quenching effect was observed from the $CH_3NH_3PbI_3$/LiSPS/$PC_{61}BM$ thin film compared to that of the $CH_3NH_3PbI_3/PC_{61}BM$ thin film, and no additional PL could be observed from either $CH_3NH_3PbI_3/PC_{61}BM$ or $CH_3NH_3PbI_3$/LiSPS/$PC_{61}BM$ thin films. Such significant PL quenching indeed confirms that efficient electron extraction takes place in the $CH_3NH_3PbI_3$/LiSPS/$PC_{61}BM$ thin films, resulting in high PCEs for the pero-HSCs W/ LiSPS.

To further investigate the electrical properties of the LiSPS interfacial layer, further impedance spectroscopy (IS) was carried out to study the internal series resistances (R_S) of the pero-HSCs W/O LiSPS and the pero-HSCs W/ LiSPS. The IS analysis enabled us to monitor the detailed electrical properties of the LiSPS interfacial modification layer, which cannot be determined by direct current measurements.[67] In solar cells, the R_S is the sum of the sheet resistance (R_{SHEET}) of the electrodes and the charge-transfer resistance (R_{CT}) at the interface between the charge-extraction layer and the electrode, and the R_{CT} at the interface between the charge-extraction layer and the light-absorbing layer. In this specific study, as all device architectures were the same, the difference in the Rs could only result from a difference in the R_{CT} at the interface between the $CH_3NH_3PbI_3$ layer and the $PC_{61}BM$ EEL, that is, the difference between the $CH_3NH_3PbI_3$/LiSPS/$PC_{61}BM$ and the $CH_3NH_3PbI_3/PC_{61}BM$ structures. **Figure 9** shows the Nyquist plots of pero-HSCs with

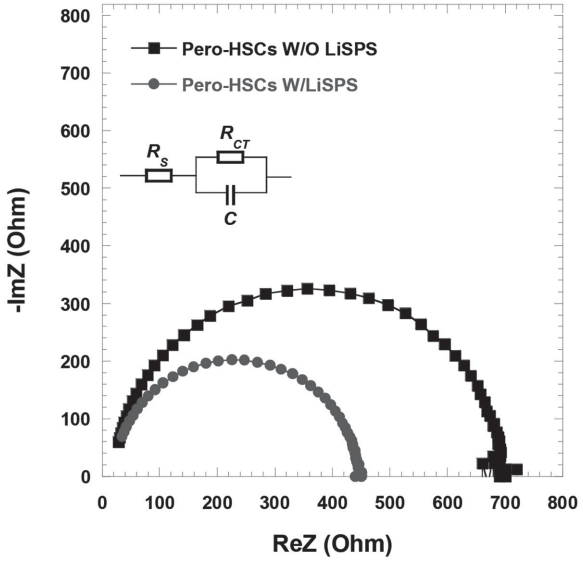

Figure 9. Nyquist plots of pero-HSCs W/O LiSPS and pero-HSCs W/ LiSPS.

and without LiSPS layer under one sun illumination and at an applied voltage close to the V_{OC} of each pero-HSC. From the plots, R_{CT} values of 700 Ω and 400 Ω could be calculated for the pero-HSCs W/O LiSPS and the pero-HSCs W/ LiSPS, respectively. The large R_{CT} value for the $PC_{61}BM/CH_3NH_3PbI_3$ indicates an inferior contact at the interface. The small R_{CT} value observed for the pero-HSCs W/ LiSPS, however, is related to the introduction of a LiSPS layer between the $CH_3NH_3PbI_3$ layer and the $PC_{61}BM$ EEL. The high ionic electrical conductive nature of LiSPS is responsible for the enhanced charge transfer properties in the pero-HSCs W/ LiSPS.

Figure 10 shows a histogram of the photovoltaic parameters of the pero-HSCs W/O LiSPS and pero-HSCs W/ LiSPS. Over 200 PHJ pero-HSCs devices were fabricated and characterized. The reproducibility of V_{OC}, J_{SC}, FF, and PCE was higher in the pero-HSCs W/ LiSPS compared to those of pero-HSCs W/O LiSPS. The average PCE was 9.43% with a relatively larger standard deviation of 1.21% for the pero-HSCs W/O LiSPS. On the other hand, the average PCE of pero-HSCs W/ LiSPS was 13.82% with a standard deviation of 0.35%, which is extremely small compared to reported values.[68] A narrow confidence interval of 13.82 ± 0.04% with a confidence level of 95% was estimated according to t-distribution calculations.[69]

Recent studies have revealed that the origin of photocurrent hysteresis can be trap states on the surface and grain boundaries of the perovskite materials.[70] The passivation of such trap states by organic materials can effectively eliminate the notorious photocurrent hysteresis.[71] In order to investigate the photocurrent hysteresis in the pero-HSCs with and without LiSPS, we carried out *J–V* measurements with different scan directions (reverse scans: from a positive to a negative bias, and forward scans: from a negative to a positive bias) and different scan rates (i.e., different delay time after each 50 mV voltage step), as shown in **Figure 11**. Previous studies have reported that large deviations were observed using different scan directions and/or delay times in pero-HSCs.[71] For pero-HSCs W/O LiSPS, the deviations between different scan directions or delay times are also typically large.[71] The best device performance was generally observed for reverse scans and the shortest or the longest delay times. However, for the pero-HSCs W/ LiSPS, the deviations between the different scan directions or delay times were dramatically decreased, which indicates that the introduction of LiSPS to re-engineer the surface of the $CH_3NH_3PbI_3$ layer might passivate the trap states

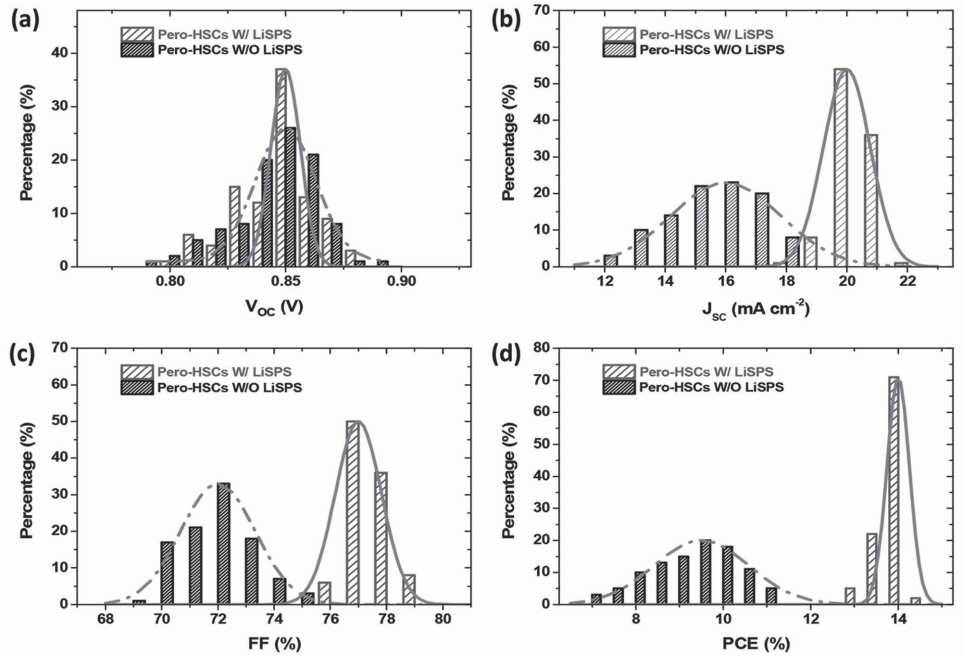

Figure 10. Histograms of photovoltaic parameters for pero-HSCs W/O LiSPS and pero-HSCs W/ LiSPS: a) V_{OC}, b) J_{SC}, c) FF, and d) PCE (the total number of devices was 200).

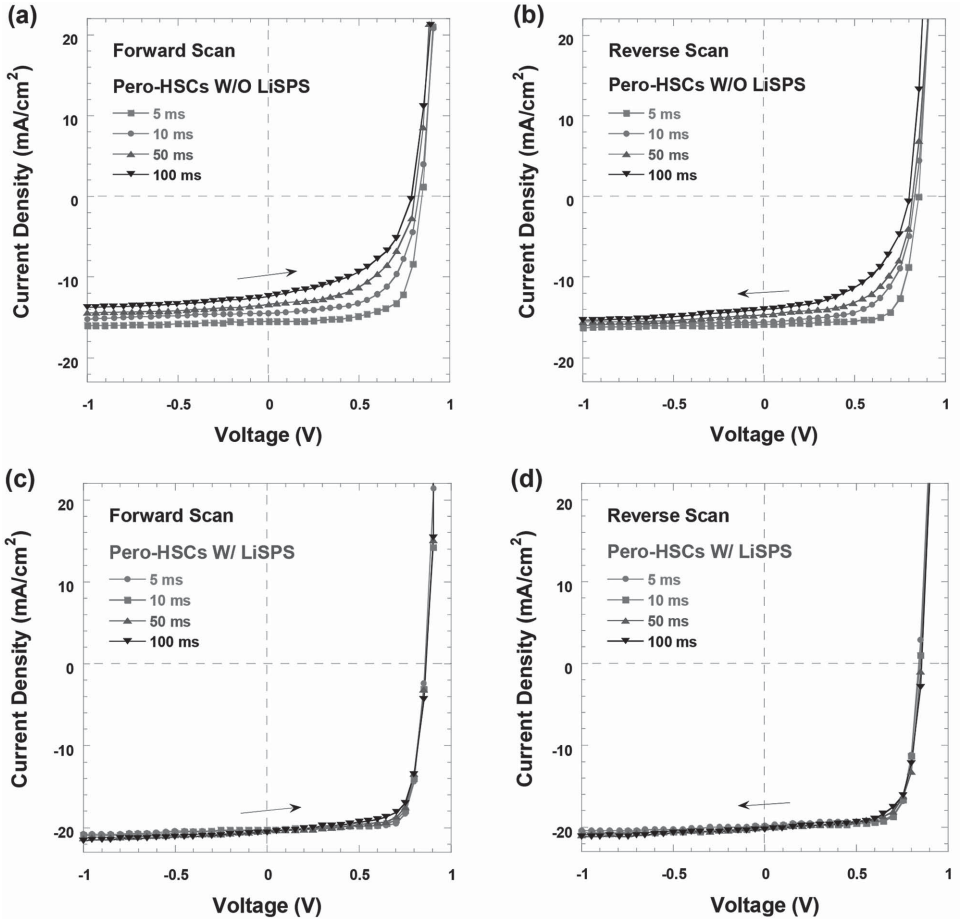

Figure 11. *J–V* characteristics of pero-HSCs W/O LiSPS and pero-HSCs W/ LiSPS under forward scan (from negative bias to positive bias) and reverse scan (from positive bias to negative bias) with different delay times of 5 ms, 10 ms, 50 ms, and 100 ms. The pero-HSCs W/O LiSPS under a) forward scan and b) reverse scan, the pero-HSCs W/ LiSPS under c) forward scan and d) reverse scan.

originating from the poor contact between the $CH_3NH_3PbI_3$ layer and the $PC_{61}BM$ EEL, resulting in the elimination of the notorious photocurrent hysteresis to a certain degree.[62]

3. Conclusion

An ultrathin ionomer layer, LiSPS, was applied to re-engineer the interface between the $CH_3NH_3PbI_3$ layer and the $PC_{61}BM$ EEL in PHJ pero-HSCs. The optimized contact between the $CH_3NH_3PbI_3$ layer and the $PC_{61}BM$ EEL via the modification with a LiSPS layer resulted in a reduced charge-carrier recombination. By filling the perforations in the $CH_3NH_3PbI_3$ layer with the LiSPS layer a reduced leakage current was obtained and the higher electrical conductivity of the LiSPS layer contributed towards more efficient charge carrier collection. As a result, the pero-HSCs incorporated with LiSPS possessed a J_{SC} of 20.90 mA cm^{-2}, a FF of 77.80%, a V_{OC} of 0.85 V, and a PCE of 13.83% with high device reproducibility and low photocurrent hysteresis. Thus, utilization of an ionomer to re-engineer the interfacial layer of solution-processed $CH_3NH_3PbI_3$ provides an efficient and simple way to approach highly reproducible and efficient pero-HSCs.

4. Experimental Section

Materials: PEDOT:PSS and $PC_{61}BM$ were purchased from Clevious and 1-Material Inc., respectively, and used as received without further purification. Lead(II) iodide (PbI_2), anhydrous *N*,*N*-dimethylformamide (DMF), ethanol (99.5%), hydroiodic acid (99.99%), and methylamine were purchased from Sigma-Aldrich and used as received without further purification. Methylammonium iodide (MAI) and LiSPS were synthesized in our labs.[28–31]

Perovskite Film Preparation: PbI_2 was first dissolved in DMF and then stirred at 70 °C for 12 hours to form a PbI_2 DMF solution with a concentration of 400 mg mL^{-1}. The PbI_2 DMF solution was then stored stably overnight to obtain a clear yellowish supernatant solution. The MAI ethanol solution was prepared by directly dissolving MAI into ethanol with a concentration of 35 mg mL^{-1}. The $CH_3NH_3PbI_3$ thin films were prepared by a two-step solution deposition method. A PbI_2 DMF solution (from a PbI_2 DMF supernatant solution at 70 °C) was firstly spin-cast on top of the pre-warmed (ca. 70 °C) substrates, followed by thermal annealing at 70 °C for 10 min, and then cooled down to room temperature. After this a MAI ethanol solution was spin-coated on top of the PbI_2 layer, followed by thermal annealing at 100 °C for 2 h to convert PbI_2 and MAI into a dark purple $CH_3NH_3PbI_3$ thin film.

LiSPS Thin Film Preparation: The LiSPS was firstly dissolved in toluene with a concentration ranging from 0.5 mg mL^{-1} to 5 mg mL^{-1}. After stirring at 75 °C overnight, LiSPS films with different thicknesses were spin-coated from the solutions with different concentrations at 6000 rpm for 30 s.

Thin Film Characterization: Top-view and cross-sectional SEM images were obtained using a field-emission scanning electron microscope (JEOL-7401). The AFM images were obtained using a NanoScope NS3A system (Digital Instrument) to observe the surface morphologies of the various thin films. The PL spectra of $CH_3NH_3PbI_3$, $CH_3NH_3PbI_3$/$PC_{61}BM$, and $CH_3NH_3PbI_3$/LiSPS/$PC_{61}BM$ thin films were performed by Picoharp 300 after preamplification. The film thicknesses were measured by a Dektak 150 surface profilometer at a scan rate of 0.06 mm s^{-1} and further confirmed by SEM. Cyclic voltammetry was carried out on a Gamry Reference 3000 instrument to measure the oxidation and reduction potentials of LiSPS. A saturated silver chloride (AgCl) electrode was employed as the reference electrode, a glassy carbon electrode and a platinum wire were used as the working and counter electrode, respectively. The CV curves were measured in an ethanol solution containing 0.1 M tetrabutylammoniumhexafluorophosphate under nitrogen atmosphere. The concentrations of LiSPS ranged from 0.50 to 1.0 mmol L^{-1}. The potentials were calibrated with respect to those of the Ag/AgCl electrode. The CV spectra are shown in Figure S1 in the Supporting Information. The energy levels of LiSPS are shown in Scheme S1 in the Supporting Information.

Pero-HSCs Fabrication: The PHJ pero-HSCs were fabricated on pre-cleaned ITO-coated glasses. The pre-cleaned ITO substrates were treated with UV-ozone for 20 minutes under ambient atmosphere. After that, a 40-nm thick film of PEDOT:PSS was spin-cast on top of the ITO substrates, followed by thermal annealing at 150 °C for 10 min under an ambient atmosphere. After this, a $CH_3NH_3PbI_3$ thin film was deposited on top of the PEDOT:PSS layer by the two-step solution-deposition method described above. The thickness of the $CH_3NH_3PbI_3$ thin film was measured to be around 300 nm. Then, an ultrathin layer of LiSPS was spin-coated from a toluene solution on top of the $CH_3NH_3PbI_3$ thin films without further thermal annealing. The thickness of the LiSPS layer was tuned by changing the concentration of the LiSPS solution and the spinning rate. The thickness of the LiSPS layer was measured to be 5 to 30 nm. Then, a 100-nm thick $PC_{61}BM$ layer was spin-cast from a chlorobenzene solution on top of either the $CH_3NH_3PbI_3$ or the LiSPS/$CH_3NH_3PbI_3$ layer. Finally, a 100-nm thick aluminum (Al) layer was thermally deposited on top of the $PC_{61}BM$ layer in vacuum at a base pressure of 6×10^{-6} mbar through a shadow mask. The device area was defined to be 0.16 cm^2.

Pero-HSCs Characterization: The *J–V* characteristics of the pero-HSCs were obtained using a Keithley model 2400 source measuring unit. A Newport Air Mass 1.5 Global (AM1.5G) full-spectrum solar simulator was applied as the light source. The light intensity was 100 mW cm^{-2}, which was calibrated by utilizing a monosilicon detector (with a KG-5 visible color filter) from National Renewable Energy Laboratory to reduce the spectral mismatch. The IPCE spectra of pero-HSCs were measured through a solar cell quantum efficiency measurement system in use at the European Solar Test Installation (ESTI) for cells and mini-modules: a 300 W steady-state xenon lamp provided the source light; up to 64 filters (8 to 20 nm width, range from 300 to 1200 nm) were available on four filter-wheels to produce the monochromatic input, which was chopped at 75 Hz, superimposed on the bias light and measured via the usual lock-in technique; the bias light was necessary to put the device under examination close to the operating irradiance condition. After collecting the IPCE data, the software also integrated the data with the AM1.5G spectrum and resulted in the calculated J_{SC} values. The Nyquist plots were extracted from impedance spectroscopy performed on an HP 4194A impedance/gain phase analyzer, under one sun illumination, with an oscillating voltage of 10 mV and frequency of 1 Hz to 1 MHz. During the recording of the impedance spectra the pero-HSCs were held at a voltage that was close to their respective open-circuit potentials obtained from the *J–V* curves.

Supporting Information

Supporting Information is available from the Wiley Online Library or from the author.

Acknowledgements

The authors thank the NSF (EECS 1351785) for financial support. K.W. appreciates the help from G. D. Deng with the AFM measurements.

Received: July 29, 2015
Revised: September 11, 2015
Published online: October 19, 2015

[1] G. A. Olah, *Angew. Chem. Int. Ed.* **2005**, *44*, 2636.
[2] J.-D. Chen, C. Cui, Y.-Q. Li, L. Zhou, Q.-D. Ou, C. Li, Y. Li, J.-X. Tang, *Adv. Mater.* **2015**, *27*, 1132.
[3] L. Zhou, Y. Li, E. Hu, J. Qin, Y. Yang, *Appl. Therm. Eng.* **2015**, *75*, 685.
[4] M. Liu, M. B. Johnston, H. J. Snaith, *Nature* **2013**, *501*, 395.
[5] J. M. Ball, M. M. Lee, A. Hey, H. J. Snaith, *Energy Environ. Sci.* **2013**, *6*, 1739.
[6] H.-S. Kim, C.-R. Lee, J.-H. Im, K.-B. Lee, T. Moehl, A. Marchioro, S.-J. Moon, R. Humphry-Baker, J.-H. Yum, J. E. Moser, M. Grätzel, N.-G. Park, *Sci. Rep.* **2012**, *2*, 591.
[7] D. Liu, T. L. Kelly, *Nat. Photonics* **2014**, *8*, 133.
[8] J. Burschka, N. Pellet, S. J. Moon, R. Humphry-Baker, P. Gao, M. K. Nazeeruddin, M. Grätzel, *Nature* **2013**, *499*, 316.
[9] G. E. Eperon, V. M. Burlakov, P. Docampo, A. Goriely, H. J. Snaith, *Adv. Funct. Mater.* **2014**, *24*, 151.
[10] K. Wang, C. Liu, P. Du, J. Zheng, X. Gong, *Energy Environ. Sci.* **2015**, *8*, 1245.
[11] C. Liu, K. Wang, P. Du, C. Yi, T. Meng, X. Gong, *Adv. Energy Mater.* **2015**, *5*, 1402024.
[12] E. Edri, S. Kirmayer, A. Henning, S. Mukhopadhyay, K. Gartsman, Y. Rosenwaks, G. Hodes, D. Cahen, *Nano Lett.* **2014**, *14*, 1000.
[13] X. Wang, L. Zhi, K. Müllen, *Nano Lett.* **2008**, *8*, 323.
[14] M. M. Lee, J. Teuscher, T. Miyasaka, T. N. Murakami, H. J. Snaith, *Science* **2012**, *338*, 643.
[15] N. Martin, A. Besnard, F. Sthal, F. Vaz, C. Nouveau, *Appl. Phys. Lett.* **2008**, *93*, 064102.
[16] F.-S. Francisco, J. Bisquert, L. Cevey, P. Chen, M. Wang, S. M. Zakeeruddin, M. Grätzel, *J. Am. Chem. Soc.* **2008**, *131*, 558.
[17] Y. Bai, H. Yu, Z. Zhu, K. Jiang, T. Zhang, N. Zhao, S. Yang, H. Yan, *J. Mater. Chem. A* **2015**, *3*, 9098.
[18] S. Ryu, J. W. Seo, S. S. Shin, Y. C. Kim, N. J. Jeon, J. H. Noh, S. I. Seok, *J. Mater. Chem. A* **2015**, *3*, 3271.
[19] C. Villeneuve-Faure, D. L. Borgne, E. Bedel-Pereira, K. M. Chane-Ching, D. Hernandez-Maldonado, I. Séguy. *J. Appl. Phys.* **2015**, *117*, 055501.
[20] D. Yoo, J. Kim, S. H. Lee, W. Cho, H. H. Choi, F. S. Kim, J. H. Kim. *J. Mater. Chem. A* **2015**, *3*, 6526.
[21] F. Xia, Q. Wu, P. Zhou, Y. Li, X. Chen, Q. Liu, J. Zhu, S. Dai, Y. Lu, S. Yang. *ACS Appl. Mater. Interfaces* **2015**, *7*, 13659.
[22] W. Tress, N. Marinova, O. Inganas, M. K. Nazeeruddin, S. M. Zakeeruddin, M. Graetzel, *IEEE Photovoltaic Spec.Conf.* **2014**, *40*, 1563.
[23] Q. Wang, Y. Shao, Q. Dong, Z. Xiao, Y. Yuan, J. Huang, *Energy Environ. Sci.* **2014**, *7*, 2359.
[24] Q. Chen, H. Zhou, Z. Hong, S. Luo, H.-S. Duan, H.-H. Wang, Y. Liu, G. Li, Y. Yang, *J. Am. Chem. Soc.* **2013**, *136*, 622.
[25] W. Zhang, M. Saliba, D. T. Moore, S. K. Pathak, M. T. Hörantner, T. Stergiopoulos, S. D. Stranks, G. E. Eperon, J. A. Alexander-Webber, A. Abate, A. Sadhanala, S. Yao, Y. Chen, R. H. Friend, L. A. Estroff, U. Wiesner, H. J. Snaith, *Nat. Commun.* **2014**, *6*, 6142.
[26] W. Nie, H. Tsai, R. Asadpour, J.-C. Blancon, A. J. Neukirch, G. Gupta, J. J. Crochet, M. Chhowalla, S. Tretiak, M. A. Alam, H.-L. Wang, A. D. Mohite, *Science* **2015**, *347*, 522.

[27] H. Zhang, H. Azimi, Y. Hou, T. Ameri, T. Przybilla, E. Spiecker, M. Kraft, U. Scherf, C. J. Brabec, *Chem. Mater.* **2014**, *26*, 5190.
[28] T. Baikie, Y. Fang, J. M. Kadro, M. Schreyer, F. Wei, S. G. Mhaisalkar, M. Graetzel, T. J. White, *J. Mater. Chem. A* **2013**, *1*, 5628.
[29] Y. Feng, A. Karim, R. A. Weiss, J. F. Douglas, C. C. Han, *Macromolecules* **1998**, *31*, 484.
[30] X. Lu, R. A. Weiss, *Macromolecules* **1996**, *29*, 1216.
[31] P. Rajagopalan, J. S. Kim, H. P. Brack, X. Lu, A. Eisenberg, R. A. Weiss, W. M. Risen, *J. Polym. Sci., Part B: Polym. Phys.* **1995**, *33*, 495.
[32] M. Guglielmi, P. Aldebert, M. Pineri, *J. Appl. Electrochem.* **1989**, *19*, 167.
[33] M. Doyle, M. E. Lewittes, M. G. Roelofs, S. A. Perusich, R. E. Lowrey, *J. Membr. Sci.* **2001**, *184*, 257.
[34] Y. V. Oza, D. R. MacFarlane, M. Forsyth, L. A. O'Dell, *Electrochim. Acta* **2015**, *175*, 80.
[35] L. Zhang, N. R. Brostowitz, K. A. Cavicchi, R. A. Weiss, *Macromol. React. Eng.* **2014**, *8*, 81.
[36] N. Espinosa, M. Hösel, D. Angmo, F. C. Krebs, *Energy Environ. Sci.* **2012**, *5*, 5117.
[37] J. Clark, D. D. Perrin, *Q. Rev. Chem. Soc.* **1964**, *18*, 295.
[38] R. D. Lundberg, H. S. Makowski, in *Ions in Polymers* (Ed: A. Eisenberg), Advances in Chemistry Series, American Chemical Society, Washington, DC, USA. **1980**, pp. 21–36.
[39] K.-G. Lim, H.-B. Kim, J. Jeong, H. Kim, J. Y. Kim, T.-W. Lee, *Adv. Mater.* **2014**, *26*, 6461.
[40] C. H. Chiang, Z. L. Tseng, C. G. Wu, *J. Mater. Chem. A* **2014**, *2*, 15897.
[41] L.-M. Chen, Z. Xu, Z. Hong, Y. Yang, *J. Mater. Chem.* **2010**, *20*, 2575.
[42] M. Bashahu, A. Habyarimana, *Renew. Energ.* **1995**, *6*, 129.
[43] D. Pysch, A. Mette, S. W. Glunz, *Sol. Energy Mater. Sol. Cells* **2007**, *91*, 1698.
[44] K. Wang, H. Ren, C. Yi, C. Liu, H. Wang, L. Huang, H. Zhang, A. Karim, X. Gong, *ACS Appl. Mater. Interfaces* **2013**, *5*, 10325.
[45] K. Bouzidi, M. Chegaar, A. Bouhemadou, *Sol. Energy Mater. Sol. Cells* **2007**, *91*, 1647.
[46] M.-S. Kim, B.-G. Kim, J. Kim, *ACS Appl. Mater. Interfaces* **2009**, *1*, 1264.
[47] O. Malinkiewicz, A. Yella, Y. H. Lee, G. M. Espallargas, M. Graetzel, M. K. Nazeeruddin, H. J. Bolink, *Nat. Photonics* **2014**, *8*, 128.
[48] H. Urabe, M. Kuramoto, T. Nakano, A. Kawaharazuka, T. Makimoto, Y. Horikoshi. *J. Cryst. Growth* **2015**, *425*, 330.
[49] J. Gilot, M. M. Wienk, R. A. Janssen, *Appl. Phys. Lett.* **2007**, *90*, 143512.
[50] F. Hao, C. C. Stoumpos, Z. Liu, R. P. Change, M. G. Kanatzidis, *J. Am. Chem. Soc.* **2014**, *136*, 16411.
[51] O. Takeuchi, N. Takeuchi, T. Ochiai, H. Kato, S. Yoshida, H. Shigekawa, *Appl. Phys. Express* **2014**, *7*, 021602.
[52] S. Slade, S. A. Campbell, T. R. Ralph, F. C. Walsh, *J. Electrochem. Soc.* **2002**, *149*, A1556.
[53] F. Berkemeier, M. Shoar Abouzari, G. Schmitz, *Appl. Phys. Lett.* **2007**, *90*, 113110.
[54] J. Shi, W. Dong, Y.-Z. Xu, C.-H. Li, S.-T. Lv, L.-F. Zhu, J. Dong, Y.-H. Luo, D.-M. Li, Q.-B. Meng, Q. Chen, *Chin. Phys. Lett.* **2013**, *30*, 128402.
[55] M. Lenes, M. Morana, C. J. Brabec, P. W. M. Blom, *Adv. Funct. Mater.* **2009**, *19*, 1106.
[56] J. You, Z. Hong, Y. M. Yang, Q. Chen, M. Cai, T.-B. Song, C.-C. Chen, S. Lu, Y. Liu, H. Zou, Y. Yang, *ACS Nano* **2014**, *8*, 1674.
[57] Z. Li, W. Wang, N. C. Greenham, C. R. McNeill, *Phys. Chem. Chem. Phys.* **2014**, *16*, 25684.
[58] C. Wehrenfennig, G. E. Eperon, M. B. Johnston, H. J. Snaith, L. M. Herz, *Adv. Mater.* **2014**, *26*, 1584.
[59] G. Xing, N. Mathews, S. S. Lim, N. Yantara, X. Liu, D. Sabba, M. Grätzel, S. Mhaisalkar, T. C. Sum, *Nat. Mater.* **2014**, *13*, 476.
[60] A. K. K. Kyaw, D. H. Wang, V. Gupta, J. Zhang, S. Chand, G. C. Bazan, A. J. Heeger, *Adv. Mater.* **2013**, *25*, 2397.
[61] S. R. Cowan, W. L. Leong, N. Banerji, G. Dennler, A. J. Heeger, *Adv. Funct. Mater.* **2011**, *21*, 3083.
[62] Z. Xiao, C. Bi, Y. Shao, Q. Dong, Q. Wang, Y. Yuan, C. Wang, Y. Gao, J. Huang, *Energy Environ. Sci.* **2014**, *7*, 2619.
[63] C. G. Shuttle, R. Hamilton, B. C. O'Regan, J. A. Nelson, J. R. Durrant, *Proc. Natl. Acad. Sci.* **2010**, *107*, 16448.
[64] L. Yao, T. Xu, W. Chen, J. M. Lee, Z. Luo, I. H. Jung, H. I. Park, S. O. Kim, L. Yu, *Nano Lett.* **2013**, *13*, 2365.
[65] Z. Wang, F. Zhang, J. Wang, X. Xu, J. Wang, Y. Liu, Z. Xu, *Chin. Sci. Bull.* **2012**, *57*, 4143.
[66] K. Wang, C. Yi, C. Liu, X. Hu, S. Chuang, X. Gong, *Sci. Rep.* **2015**, *5*, 9265.
[67] J. S. Kim, W. S. Chung, K. Kim, D. Y. Kim, K. J. Paeng, S. M. Jo, S. Y. Jang, *Adv. Funct. Mater.* **2010**, *20*, 3538.
[68] Z. Wu, S. Bai, J. Xiang, Z. Yuan, Y. Yang, W. Cui, X. Gao, Z. Liu, Y. Jin, B. Sun, *Nanoscale* **2014**, *6*, 10505.
[69] K. L. Lange, R. J. Little, J. M. Taylor, *J. Am. Stat. Assoc.* **1989**, *84*, 881.
[70] H. J. Snaith, A. Abate, J. M. Ball, G. E. Eperon, T. Leijtens, N. K. Noel, S. D. Stranks, J. T.-W. Wang, K. Wojciechowski, W. Zhang, *J. Phys. Chem. Lett.* **2014**, *5*, 1511.
[71] Y. Shao, Z. Xiao, C. Bi, Y. Yuan, J. Huang, *Nat. Commun.* **2014**, *5*, 5784.